Constraining the Degree of Alignment between the Spin of Black Hole XTE J1550–564 and the Angular Momentum of its Host Binary

James F. Steiner[1] and Jeffrey E. McClintock[1]

jsteiner@cfa.harvard.edu

ABSTRACT

The spins of nine stellar-mass black holes have been estimated by fitting their X-ray continuum spectra to a relativistic accretion disk model. In order to obtain reliable spin results by this method, it is essential to have an accurate value for the inclination of the inner, X-ray-emitting portion of the disk, which (via the Bardeen-Petterson effect) will be the same as the inclination of the black hole's spin vector. In practical applications of the continuum-fitting method, one uses the inclination of the orbital plane of the host binary, as determined from optical observations. That is, one assumes that the black hole's spin axis (and hence the jet axis) is aligned with the orbital vector. The microquasar XTE J1550–564 offers a near-unique opportunity to test this assumption. Building on earlier work and using *Chandra* and radio images, we have modeled the kinematic motion of the ballistic jets of this microquasar and determined the degree of alignment. Our jet model gives a high inclination for the black hole's spin axis, $\theta > 65°$. Comparing this constraint with the inclination of the orbital plane, we find that the spin and orbital vectors are misaligned by < 12 deg (90% confidence).

Subject headings: black hole physics — stars: individual (XTE J1550–564) — X-rays: binaries

1. Introduction

Although it is thought that the Galaxy is host to tens of millions of stellar-mass black holes, only about 50 have been discovered (Özel et al. 2010). All of them are accretion-powered X-ray sources that are located in X-ray binary systems. Most such systems, which

[1]Harvard-Smithsonian Center for Astrophysics, 60 Garden Street, Cambridge, MA 02138.

are similar to our featured black-hole binary XTE J1550–564, have short orbital periods ($P \sim 1$d) and are comprised of a low-mass ($\lesssim 1\mathrm{M}_\odot$) donor star and a $\sim 10\mathrm{M}_\odot$ black hole. A stream of gas from the Roche-lobe-filling star feeds into the outer part of an accretion disk that encircles the black hole. On a time scale of weeks, viscous forces in the disk cause gas to move radially inward to the center. Within a few hundred kilometers of the black hole, the optically-thick gas reaches a temperature of $\sim 10^7$K and produces an X-ray luminosity that is near the Eddington limit ($L \sim 10^{39}$ erg s^{-1}). Accretion onto the black hole is not a steady process: A typical source is luminous for only about a year, and then deeply quiescent for years or decades.

XTE J1550–564 (hereafter J1550) is a much-studied Galactic black-hole transient system that was discovered on 1998 September 6 using the All-Sky Monitor (ASM) on board the *Rossi X-ray Timing Explorer (RXTE)*. Thereafter, it was observed almost daily during its entire 8-month outburst cycle using RXTE's pointed instruments (Sobczak et al. 2000). Two weeks into outburst, the source produced a brilliant 7-Crab flare corresponding to a fourfold increase in intensity, during which the source was at or near its Eddington limit for ≈ 1 day. Four days later, radio observations made using the Australian Long Baseline Array (LBA) revealed relativistic ejecta moving both eastward and westward from J1550. The two components were observed to be separated by ~ 250 mas and moving at relative speed of $\mu_{\rm app} \approx 65$ mas/d, equivalent to an apparent separation velocity of ~ 1.66c (Hannikainen et al. 2009). Nearly two years later, *Chandra* imaging observations revealed large-scale ($\gtrsim 20''$) relativistic jets undergoing deceleration. This landmark discovery of a pair of ballistic X-ray jets was the first detection of its kind for a Galactic source.

By modeling an extensive collection of optical and infrared data for J1550, Orosz et al. (2011) have determined the mass of the black hole primary, $M_{\rm BH} = 9.1 \pm 0.6\mathrm{M}_\odot$, the distance to the binary, $D = 4.38^{+0.58}_{-0.41}$ kpc, and the inclination of its orbital plane, $i = 74.^\circ7 \pm 3.^\circ8$. Assuming that the black hole's spin is aligned with the orbital angular momentum, Steiner et al. (2011) have measured the spin using the continuum-fitting method to be $a_* = 0.34^{+0.20}_{-0.28}$, where $a_* \equiv cJ/GM^2$ is the blacktimescale hole's dimensionless spin parameter and J its angular momentum. Steiner et al. also measured the spin using the independent Fe-line method and find $a_* = 0.55^{+0.10}_{-0.15}$; taken together, the two measurements imply $a_* \approx 0.5$. In constraining spin via either the continuum-fitting or Fe-line methods, one relies respectively on a model for the thermal emission from an accretion disk (Zhang et al. 1997) or a model of the relativistically broadened fluorescence features emitted by the disk (Fabian et al. 1989).

For a low-mass black-hole binary system like J1550, the ratio of orbital- to spin-angular momentum is given by

$$J_{\rm orb}/J_{\rm spin} \approx 65.4\ a_*^{-1} \left(\frac{M_{\rm BH}}{10\ {\rm M}_\odot}\right)^{-4/3} \left(\frac{M_2}{{\rm M}_\odot}\right) \left(\frac{P}{1\ {\rm d}}\right)^{1/3}, \quad (1)$$

where M_2 is the mass of the secondary star. For J1550, this ratio is $\sim$50, and thus it is reasonable to expect that given a means of interaction, the black hole's spin will eventually come into alignment with the orbital angular momentum. The timescale for this to occur is an important question for the continuum-fitting method, which usually assumes that the two vectors are aligned.

If there is an initial misalignment between the spin and the orbital angular momentum, then Lense-Thirring precession will cause the inner X-ray-emitting portion of the disk to line up with spin of the black hole (Bardeen & Petterson 1975). At the same time, at very large scales, the disk will align itself with the orbital plane, and the transition between these regimes will manifest as a warp in the disk. If any misalignment is present, the black hole will be torqued into alignment by the accreting matter acting with a lever arm of order the warp radius (e.g., Natarajan & Pringle 1998). Using the most conservative (minimum-torque) assumption, Fragos et al. (2010) carried out a population synthesis study and concluded that most black holes in binary systems will be tilted less than 10°. Fragos et al. assumed that the torque acts at the inner-most stable circular orbit, $R_{\rm ISCO} = 6GM/c^2$ for $a_* = 0$, whereas the warp radius has been estimated to be $R_{\rm w} \approx 200GM/c^2$ (King et al. 2005; Lodato & Pringle 2006).

The timescale for accretion to torque the black-hole into alignment has been variously estimated as $t_{\rm align} \sim 10^6 - 10^8$ years (Martin et al. 2009; Maccarone 2002[1]). For a typical black-hole binary, alignment should occur after just a few percent of the binary lifetime, so that most observed systems will be well aligned. However, given that tens of black-hole systems are known, based upon extrapolations from the supernova kicks imparted onto neutron star systems, it is expected that one or even a few may harbor a black hole which is significant tilted with respect to the binary orbital plane.

While this expectation is set by theory, it remains observationally challenging to identify misaligned systems and even to measure the degree of alignment in a particular source. Usually the inclination of the binary orbital plane is measured by modeling ellipsoidal orbital variations of the secondary star (e.g., Orosz et al. 2009). But it is very difficult to measure

[1]A numerical error in Eqn. 6 of Maccarone (2002) causes an overestimate of $t_{\rm align}$ by a factor $\approx$ 50, compared to what is implied using their Eqn. 1.

the orientation of the spin axis of the source. In principle, the Fe-line model used to measure spin can constrain the inclination of the inner disk (Reynolds & Nowak 2003) which is aligned to the spin axis via the Bardeen-Petterson effect. Presently, however, this approach is not yet robust because simplifications inherent in the models result in a degeneracy between the inclination angle and the ionization state of iron over the disk. The prospects are good that more advanced Fe-line models will eventually yield reliable estimates of inner-disk inclination, which can be compared to the inclination of the orbital plane. At present, the most direct way to determine the inclination of the inner disk is by model jet ejecta, which are presumed to be aligned with the black hole's spin axis. For the case of symmetric jets, see the review by Mirabel & Rodríguez (1999).

Based upon the motion of relativistic jets produced during X-ray outbursts, two systems are good candidates for hosting misaligned black holes: GRO J1655–40 and SAX 1819–2525[2]. During outburst, the former produced a sequence of jet plasmons which showed correlation with a series of X-ray flares. These ejecta were tracked by two groups, Hjellming & Rupen (1995) and Tingay et al. (1995), who reported proper motions of 54 and 45, and 65 ± 5 mas/d, respectively. While the precise jet trajectories are ambiguous, the motions adopted in Hjellming & Rupen (1995) indicate that the black hole is nominally tilted by $\approx 15^\circ$ relative to the binary orbit, and at 85° to the line of sight. The case is less certain for SAX 1819–2525, in which just one observation of extended radio emission was taken and associated with an X-ray outburst hours earlier, implying highly superluminal motion: $\beta_{\rm app} > 10c$, and a misalignment $> 50^\circ$ (Orosz et al. 2001; Hjellming et al. 2000). The radio plasmon rapidly faded and was not seen upon repeated observations days later, and Chaty et al. (2003) have speculated that the radio jet may have been launched several days preceding the X-ray flaring, while the source was optically active. Motivated by these ostensible misalignments, a pair of warped disk models have been developed which illustrate the time-evolution of the alignment and disk in each system by Martin et al. (2008b) on GRO J1655–40 and Martin et al. (2008a) on SAX 1819–2525.

Compared to these two systems and the other Galactic microquasars, the remarkable jet ejections in J1550 stand out. For one, the jet ejecta become bright at very late time after outburst; this long timeframe is also the reason that the jets appear at a very large physical separation from one another. In fact, when considering a dimensionless scale by which to measure the size of black-hole jets (R/M), the J1550 jets may well be the largest observed from any back hole (Hao & Zhang 2009, and see Heinz 2002), and would correspond to a jet radius of 1–10 Mpc from a supermassive black hole.

---

[2]Another system, SS 433 shows evidence of a tilted spin axis, but whether its compact primary is a black hole or a neutron star is uncertain.

In a previous study, Wang et al. (2003) modeled the light curve and dynamical evolution of J1550's ballistic jets using the same model we employ. Namely, one of an expanding jet interacting with the interstellar medium (ISM). They applied this model to X-ray observations of J1550's eastern jet and thereby determined that the gas density around J1550 is unusually low and also that the X-ray emission is attributable to a reverse shock propagating back through the jet front. Later, their work was extended to include the western jet by Hao & Zhang (2009). Both groups focused their modeling efforts on the properties of the environment around J1550. Accordingly, Wang et al. (2003) and Hao & Zhang (2009) adopted nominal and fixed values for the jet inclination (50° and 68° respectively), initial Lorentz factor (3), and jet energy (3.6×10^{44} erg). With these assumptions, both groups found evidence for the existence of a low density cavity around J1550 (modeled in more detail by Hao & Zhang), and a possible asymmetry in the ambient gas in the eastern and western fronts.

In this Paper, we adopt a similar procedure but with the specific aim of testing the alignment of the black hole with its binary plane. Because the light curves are mostly useful to constrain the electron and magnetic field distributions in the jet lobes, and also because the emission mechanisms may be variable and multiple, we disregard the light-curve data. Instead, we focus upon modeling the dynamics of the ballistic jets and carefully deriving reliable values and error estimates for each of the parameters. Ultimately, we use our inference about the inclination of J1550's spin-axis to constraint its possible misalignment.

2. Data

We use archival *Chandra X-ray Observatory* data for eight observations of J1550 that were obtained using the Advanced CCD Imaging Spectrometer (ACIS) between 2000 June and 2003 October. The exposure times range from $\approx 4 - 50$ ks. Pipeline processed level-2 event files[3] were used to produce images of the field of J1550. When detected, images of the eastern (approaching) jet yielded 16–40 counts and the western (receding) jet 100–400 counts; J1550 itself was always detected and yielded 60–3000 counts.

These same *Chandra* data were used by Hao & Zhang (2009) in their analysis of the X-ray jets. They relied on the absolute astrometric precision of *Chandra* in order to derive positions for each lobe and thereby its offset from J1550. We have reduced the astrometric errors severalfold by directly measuring the relative separations between J1550 and the jet lobes in each image.

[3]using CXC DS-7.6.10

In order to measure the precise jet positions, which are given in Table 1, we smoothed each image using a $1''$ Gaussian kernel and then determined the centroid of each jet lobe using the DAOphot FIND routine (Stetson 1987). This procedure was used to derive initial estimates for all the jet positions. Then, 1000 Poisson random realizations of each field were produced, and the centroid measurements were repeated. In most cases, the positions for a given lobe were tightly clustered about a single value, and a separation and error were derived from this distribution. However, in the case of three faint images, the eastern jet was dim (possibly because the emission is extended), which resulted in a broad distribution of positions (Obs. X1, X3, and X5 in Table 1). In these cases, a Gaussian-weighted mean was used to derive the offset by using weights w_j obeying $\log(w_j) = -\frac{1}{2}(\phi_j - \phi_{\rm PA})^2/\sigma^2_{\rm PA}$. Here, we used a fixed position angle which was measured using a coaligned, coadded frame to be $\phi_{\rm PA} \approx 94^\circ.25 \pm 0^\circ.3$, consistent with the position angle determined by both Hannikainen et al. (2009) and Corbel et al. (2002). Typically, the position errors for the eastern jet were several tenths of an arcsec, while for the brighter western jet they were $\lesssim 0.1''$.

In addition to the positions derived using the *Chandra* data, we include in our analysis two radio positions (Obs. R1 and R2 in Table 1). These measurements are taken from Corbel et al. (2002), who derived positions from observations by the Australia Telescope Compact Array (ATCA) taken on 2000 June 1 and 2002 January 29. In the first observation, only the eastern jet is observed, whereas in the second, the eastern jet has faded and the western jet alone is present.

As a final constraint on our kinematic jet model, we require that the apparent separation speed of the jets at launch match the value measured using the LBA, 65.5 ± 13.2 mas/d Hannikainen et al. (2009). This speed and the jet positions are the sole inputs to our principal model in § 5. However, we also consider radio intensity measurements given by Hannikainen et al. (2009) in § 6. They report 2.29 GHz flux densities taken four and six days after the X-ray flare with intensity ratios of $S_{E1}/S_{W1} = 3.55$ and $S_{E2}/S_{W2} = 2.40$, respectively; we assume uncertainties of 25% for both measurements. We also adopt their measurements of the radio spectral index, $\alpha_1 = -0.43$ and $\alpha_2 = -0.21$, taken from flux densities measured with the ACTA at 4.8 and 8.6 GHz. The spectral index measurements and corresponding LBA images, while not strictly simultaneous, were obtained within several hours of each other.

3. The Jet Model

The development of our kinematic jet model follows Hao & Zhang (2009) and Wang et al. (2003). The model we use has been designed to describe gamma-ray bursts, but it

is broadly applicable to the general case of a relativistic, adiabatically expanding jet and accompanying shock wave. To begin, we consider a pair of symmetric jets, each launched with a kinetic energy E_0 and Lorentz factor Γ_0. As the jets expand into their environments, they entrain material from the surrounding medium and dissipate their kinetic energy at the shock front, heating the ISM. We neglect radiative losses, and assume the jets are confined and evolve adiabatically. The jets obey

$$E_0 = (\Gamma - 1)M_0c^2 + \sigma(\Gamma_{\rm sh}^2 - 1)m_{\rm sw}c^2, \tag{2}$$

where Γ is the instantaneous bulk Lorentz factor of the jet, M_0 is the mass of the jet ejecta, and $\Gamma_{\rm sh}$ is the Lorentz factor at the shock front. The mass of the entrained material, $m_{\rm sw}$, that has been swept up by the shock is approximately $m_{\rm sw} = \Theta^2 m_{\rm p} n \pi R^3/3$, where Θ and R are respectively the half opening angle and the distance the jet has traveled. The numerical factor σ varies from ≈ 0.35 for ultrarelativistic shocks to ≈ 0.73 in the nonrelativistic limit (Wang et al. 2003; Blandford & McKee 1976). Following Huang et al. (1999), we adopt a simple numerical scaling to interpolate between the two regimes: $\sigma = 0.73 - 0.38\beta$, ($\beta = \sqrt{1 - 1/\Gamma^2}$).

At the shock front, the jump condition relates the bulk Lorentz factor in the jet to that of the shocked gas:

$$\Gamma_{\rm sh}^2 = \frac{(\Gamma + 1)[\hat{\gamma}(\Gamma - 1) + 1]^2}{\hat{\gamma}(2 - \hat{\gamma})(\Gamma - 1) + 2}. \tag{3}$$

The adiabatic index $\hat{\gamma}$ varies between 4/3 and 5/3, which are respectively its ultrarelativistic and nonrelativistic limits. We interpolate between these regimes via $\hat{\gamma} = (4\Gamma + 1)/3\Gamma$ (Huang et al. 1999; Wang et al. 2003; Hao & Zhang 2009).

The apparent (projected) motions of the approaching and receding jets are given by

$$\mu_{\rm a} = \frac{\beta\ c\ \sin\theta}{D(1 - \beta\ \cos\theta)}, \qquad \mu_{\rm r} = \frac{\beta\ c\ \sin\theta}{D(1 + \beta\ \cos\theta)}. \tag{4}$$

As we show in § 5, this simplistic model fails to describe the data. Motivated by the results of Hao & Zhang and Wang et al., we have generalized Eqn. 2 to allow for the jet to propagate freely through a low-density cavity before shocking against the much higher density ISM. We also allow for the size of this cavity to differ from east to west, and also for the presence of intrinsic asymmetry in either the two jet lobes or in the gas density from east to west. Eqn. 2 becomes:

$$\eta E_0 = (\Gamma - 1)\eta M_0c^2 + \sigma(\Gamma_{\rm sh}^2 - 1)m_{\rm sw}c^2, \tag{5}$$

where the entrained mass is now

$$m_{\rm sw} = \frac{\Theta^2 m_{\rm p} n \pi}{3} \times \begin{cases} R^3, & R \le \zeta R_{\rm cr}, \\ (\zeta R_{\rm cr})^3 + \delta[R^3 - (\zeta R_{\rm cr})^3], & R > \zeta R_{\rm cr} \end{cases} \tag{6}$$

where $R_{\rm cr}$ and δ are respectively the radius of the cavity centered on J1550 and the density jump at the cavity boundary. The asymmetry in the jet (or alternatively the ambient medium) and the cavity are described by the parameters η and ζ, respectively. Both of these parameters are fixed to unity for the eastern jet, but may be allowed to vary for the western jet.

While solving Eqns. 5 and 6 for the observed separation on the sky, each solution uses a subset of eight possible parameters: θ, Γ_0, D, $R_{\rm cr}$, δ, η, ζ, and lastly the "effective energy" $\tilde{E}$. There is a degeneracy in the model in which the energy term is inseparable from the density and opening angle; the model treats the combined quantity $E_0/n\Theta^2$ as a single parameter. To make physical sense of this, we assume that the density of the ISM is a standard $n_{\rm ISM} = 1$ cm^{-3} so that $n = 1/\delta$ cm^{-3} and adopt $\Theta = 1^\circ$ (Kaaret et al. 2003). Predicated upon our assumed values for $n_{\rm ISM}$ and Θ, the energy is taken to be $\tilde{E}$.

Finally, in going beyond our principal model to consider the ratio of jet intensities, the case of symmetric lobes at equal separation is given by (Mirabel & Rodríguez 1999):

$$\frac{S_a}{S_r} = \left(\frac{1+\beta\,\cos\,\theta}{1-\beta\,\cos\,\theta}\right)^{k-\alpha}, \tag{7}$$

where sub-indexes a and r refer to the approaching and receding lobes and k ranges from 2 for continuous jets to 3 for discrete ejecta. Since our observations provide snapshots at a fixed time but unequal separation, we allow for additional time dependence in the brightness of the jets, and parameterize their evolution as a power-law in time from the jets' rest frame. Then, Eqn. 7 becomes

$$\frac{S_E}{S_W} = \left[\frac{\Gamma_W(1+\beta_W\,\cos\,\theta)}{\Gamma_E(1-\beta_E\,\cos\,\theta)}\right]^{k-\alpha-\Delta}\eta^q, \tag{8}$$

where Δ is a fit parameter and for positive values describes a decay in brightness with time. The effect of asymmetry is captured by q, which can range from -1 to 1.5 depending on whether E_0, n, or Θ is the source of asymmetry.

4. Markov Chain Monte Carlo

Markov Chain Monte Carlo (MCMC) is a powerful statistical technique by which random samples may be drawn from a posterior distribution of unknown form. In our case, the posterior distribution is the probability of our model parameters, given the data. MCMC algorithms perform a "guided walk" through parameter space such that, after an initial burn-in phase, the chain directly reproduces the likelihood surface for the model. The chain itself is simply an ensemble of points in parameter space with the special property that the

density of chain elements within a finite volume of parameter space is proportional to the likelihood surface integrated over that volume. MCMC has several advantages over traditional gridded-search algorithms when the number of parameters is large. For example, the search time with MCMC scales approximately linearly with the number of parameters rather than exponentially (Martínez et al. 2009). Furthermore, the ergodic property of the Markov Chain guarantees (asymptotically) that the chain will fully explore parameter space, ensuring that a true global optimization is found.

We implement a particular class of the algorithm known as random-walk MCMC. In this approach, a sequence of transitions from the current parameter values are proposed and incrementally accepted or rejected. These transitions are effected via a "jump" distribution $J(x^*|x_n)$ (e.g., a multivariate Gaussian) that defines a probability of transitioning to a new state x^* given the current state x_n. The transition from x_n to x^* is governed by the Metropolis-Hastings algorithm (Hastings 1970) and is determined by the ratio of probability densities r

$$r = \frac{p(x^*|y)J(x_n|x^*)}{p(x_n|y)J(x^*|x_n)}, \tag{9}$$

where y refers to the data, and $p(a|b)$ should be read in the usual way as the probability of a given b. The term $p(x^*|y)/p(x_n|y)$ in the equation above gives the likelihood ratio of the two states, while the remaining term corrects for bias introduced by the jump distribution density at each state. The state of the next link in the chain, x_{n+1}, is then chosen according to

$$x_{n+1} = \begin{cases} x^*, & \text{with probability } \min[r, 1], \\ x_n, & \text{otherwise.} \end{cases} \tag{10}$$

The likelihood ratio appearing in Eqn. 9 is calculated by evaluating the χ^2 for each state while taking into account the prior $\wp$ on all of the model parameters. In this case, the priors are introduced independently so that $\wp \equiv \prod_{k=1}^{\mathrm{N}} \wp_k$, where N is the number of parameters and $\wp_k$ gives the prior for parameter k. Omitting additive constants, the log-likelihood for state x is

$$\log\left(p(x|y)\right) = -\frac{1}{2}\left[\chi^2(x) - 2\,\log\left(\wp(x)\right)\right]. \tag{11}$$

4.1. MCMC in Practice

As Eqn. 11 makes apparent, the prior acts as a penalty to χ^2, and for the special case that a prior is "flat" (i.e., independent of x), one recovers the usual least-squares formula. It is also worth noting that because the prior only enters into the MCMC chain generation as a

ratio (Eqn. 9) the scaling of the prior is arbitrary. We introduce a new term for this penalized χ^2, $\chi^2_\wp$. While generally only differences in $\chi^2_\wp$ are used to assess the relative performance of a model, unless stating otherwise, we will choose a normalization for the prior so that the penalty term is zero at the best fit. (The best fit is at the minimum $\chi^2_\wp$, which is also the maximum likelihood.)

Priors can be viewed as a means of accounting for the likelihood of obtaining a certain parameter value without regard to how well the data are fitted. For example, we adopt a split-Gaussian prior on the distance because it has been previously measured using optical and near-infrared photometry (see § 1, also Orosz et al. 2011). For the asymmetric terms, we adopt a flat prior on the logarithmic deviation from unity, i.e., $\wp_\eta \propto \min[1/\eta, \eta]$ (where we use the same expression for $\wp_\zeta$). Stated differently, we consider a term implying a 10-fold asymmetry to be *a priori* one tenth as likely as one that is symmetric. We adopt flat priors on inclination θ and $R_{\rm cr}$ and flat priors on the log-values of scale parameters (i.e., the jet energy, Γ_0 and δ).

While it is optimal to use an unbounded parameter space in performing MCMC sampling, it is also sensible to set physically meaningful constraints on the parameters (e.g., $\Gamma_0 > 1$). To achieve both, we have transformed each parameter using a logit function to map a parameter range $[z_{\rm min}, z_{\rm max}]$ onto an infinite scale:

$$\mathrm{logit}(t) \equiv z_{\rm min} + \frac{z_{\rm max} - z_{\rm min}}{1 + e^{-t}}, \qquad -\infty < t < \infty, \tag{12}$$

for a parameter, z. The parameter ranges are listed in Table 2.

We initialize the chain with starting guesses for both the model parameters and also for the step sizes used to set a multivariate-normal jump distribution. However, this initial guess for the jump function almost always results in poor sampling of the parameter space and computation times that are often prohibitively long. This situation can be remedied, however, by running a sequence of "training" iterations. These training iterations provide increasingly precise measurements of the likelihood structure, produce refined estimates for the parameter covariance matrix Σ, and ultimately result in the samples converging upon the maximum likelihood. For each training chain, the covariance matrix is used to define a jump function as a $t-$distribution with 4 degrees of freedom. (The $t-$distribution is similar to a Gaussian, but it has broader wings to improve mixing.) These refinements iteratively sculpt the jump function until it is an excellent approximation to the posterior covariance matrix, thereby greatly increasing the efficiency of the MCMC process.

The training phase was employed for a minimum of 15 iterations, each of which generated 2000 links. Training terminated either after 25 cycles were completed or when the chain

attained an acceptance fraction ("movement") between $24\% - 37\%$[4]. Each run produced an acceptance fraction of at least 20%.

Upon completing its training cycle, 8 chains were generated and run in parallel using the trained jump function, each to a length of 110 thousand elements. Seven of the starting positions were chosen using a dispersed 10 Σ covariance about the final position in the training sequence, and the eighth was started directly from the end location reached by the training sequence. The initial 10 thousand elements of each chain were rejected because they were generated during a "burn-in" phase in which the chains relax toward the desired stationary distribution. Our final results are based on a total of 8×10^5 MCMC samples. Convergence of the MCMC run is assessed using the criterion of Gelman & Rubin (1992), which measures the ratio of the inter-chain variance to the intra-chain variance: the closeness of this criterion to unity is the measure of convergence.

In Figure 1 we plot a trace of our parallel runs over time for inclination in our adopted model (see § 5). In the bottom panel, we show the Gelman & Rubin convergence diagnostic of the chain over time. Typically, a convergence threshold $\hat{R} \leq 1.1$ or 1.2 is used (see, e.g., Verde et al. 2003). Larger values of $\hat{R}$ suggest that either the parameter space is insufficiently sampled or that the chains are not fully evolved. We obtain $\hat{R} < 1.01$ for θ, our parameter of interest.

5. Results

To begin with, we first consider and rule out two simple models. We start by assuming the simplest case, which we refer to as Model S1, in which the jets are symmetric and propagating through a uniform medium (i.e., $\eta = \zeta = \delta = 1$ and $R_{\rm cr} = 0$). The best fit achieved by this simple model yields an unacceptable $\chi^2_\wp/\nu = 68$. The strong curvature implied by the data at late times is simply incompatible with the unabated motion early on. Next, we introduce a symmetric cavity centered on J1550 (δ and $R_{\rm cr}$ are free fit parameters). This formulation, Model S2, attains $\chi^2_\wp/\nu = 41$, a significant improvement but still far from an acceptable fit. Results from both models are shown in Table 2.

By introducing a modest $\sim 25\%$ asymmetry in the size of the jet cavities (Model AC), we are able to produce a successful fit to the data; this model is shown in Figure 2 with goodness value $\chi^2_\wp/\nu = 1.65$. In this case, ζ is a free fit parameter, while η is still fixed to

[4]The optimal movement was set at $\approx 32\%$. This value ranges from $\approx 23\%$ for an infinite-dimensional problem to $\approx 45\%$ for a univariate problem (Gelman et al. 1996).

Table 1. J1550 Jet Positions

Obs.	Δt[a]	Eastern Lobe (arcsec)	Western Lobe (arcsec)
R1	620.5	21.9±0.3[b]	···
X1	628.5	21.5±0.5	···
X2	701.4	22.7±0.2	···
X3	722.2	23.7±0.5	···
R2	1227.5	···	22.6±0.3[b]
X4	1268.8	28.5±0.2	22.78±0.05
X5	1368.5	···	23.19±0.07
X6	1466.0	29.6±0.6	23.44±0.10
X7	1591.3	···	23.76±0.10
X8	1859.6	···	24.4 ±0.2

[a]Time since the jets were launched, equal to MJD - 51076.0.

[b]ACTA position from (Corbel et al. 2002).

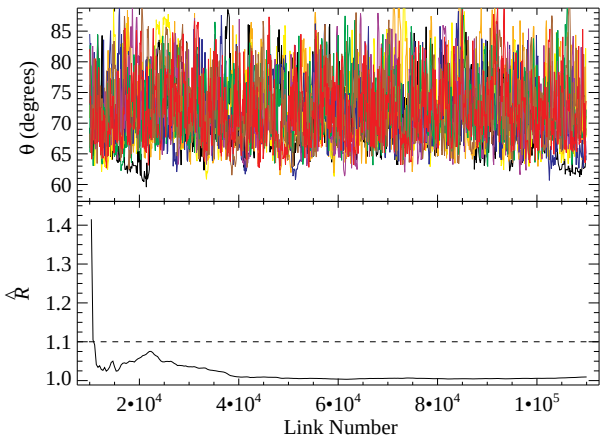

Fig. 1.— *top*: The trace of θ for Model AC of § 5. Eight parallel chains are used, and for each the initial 10^4 elements are thrown out for the burn-in phase. *bottom*: The convergence of the chain over time. The chains reach convergence quickly, which is indicative of good mixing.

unity. The modeling results are summarized in Table 2 and marginal MCMC distributions for each parameter are shown in Figure 3. We find that the cavity surrounding J1550 extends out to 0.6 pc (eastern side) and 0.5 pc (western side) from the black hole, and that at the cavity boundary there is a density contrast ~ 100. This implies that both jets freely expanded with very low mass-loading for the first ≈2–3 years. But because the western cavity is significantly smaller, the receding jet reached the dense ISM earlier (from the frame of J1550) and therefore decelerated more rapidly than its eastern counterpart as it accumulated mass.

The MCMC results constrain the launching speed of the jets to values greater than $\Gamma_0 = 1.6$ (3σ), but at large Γ_0, the data provides essentially no constraint and so the distribution closely tracks the prior (Fig. 3). The distance is likewise only weakly informed by the data and mostly follows the prior distribution. The remaining parameters are determined by the data and have only minor dependence on the prior. The jet angle is measured as $\theta \approx 71^\circ$, and shows moderate correlation with the other fit parameters. The strongest two of these correlations are with ζ, and with $R_{\rm cr}$, shown in Figure 4.

We adopt Model AC as the most likely explanation for J1550's jet evolution, with which we can test the degree to which J1550's spin (jet) and the binary orbital axes are misaligned. Using a Gaussian distribution of the binary inclination, $i = 74.7 \pm 3.^\circ 8$ from Orosz et al. (2011), we compute the difference between the binary plane and the jet axis. From the distribution of tilt estimates, we find (Fig. 5) no evidence for misalignment; the results are consistent with $\theta = i$, and we place 1σ and 90% upper limits on the degree of misalignment at 8° and 12°, respectively.

6. Radio Intensities and Asymmetric Jets

Motivated by the alternating intensity ratios in the jets of GRO J1655–40, wherein the approaching and receding sides may each be the dominant source of synchrotron emission at different times (Hjellming & Rupen 1995; Mirabel & Rodríguez 1999), we now consider the radio intensity measurements of J1550's jets with two aims: We wish to identify any intrinsic asymmetry in the jet and at the same time check the consistency of our dynamical result. To this end, we first re-fit our adopted kinematic model again assuming asymmetric cavities, but we now introduce the two radio intensity measurements and the additional free parameter Δ to describe the decay rate of the jet emission over time; we refer to this as Model RAC. The modeling results for Model RAC are nearly the same as for Model AC, with the jet inclination settling at a slightly larger value. The fit is quite good: $\chi^2_\wp/\nu = 1.38$, and Δ is positive ($\Delta \approx 1 - 5$).

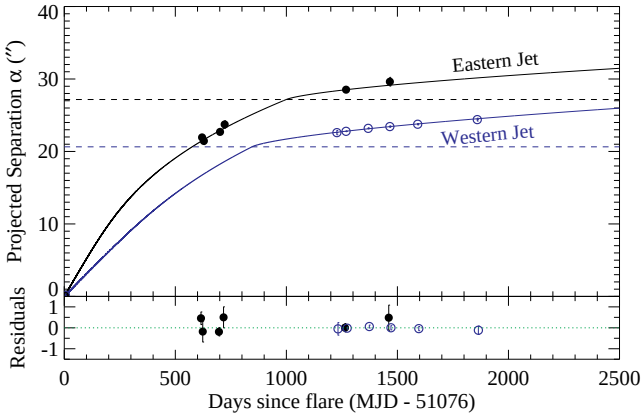

Fig. 2.— The best-fitting model and fit residuals for the eastern jet (black) and western jet (blue). The cavity locations are marked by dashed horizontal lines, indicating that the western wall (for the receding jet) is smaller than that for the eastern jet.

Table 2. Kinematic Model Settings and Fit Results

Parameter	Range	Prior Shape[a]	Model S1	Model S2	Model AC
θ (degrees)	$0 - 89.99$	F	53.9 ± 0.7	58.16 ± 1.7	$70.8^{+7.3}_{-4.5}$
Γ_0	$1 - 1000$	LF	210^{+390}_{-160}	50^{+320}_{-43}	36^{+300}_{-32}
$\tilde{E}$ (10^{45} erg)	$10^{-10} - 10^{10}$	LF	$91.8^{+9.6}_{-6.7}$	74^{+18}_{-14}	$5.9^{+3.6}_{-2.3}$
D (kpc)	$3 - 7$[b]	N($4.38^{+0.58}_{-0.41}$)	3.07 ± 0.06	$4.30^{+0.29}_{-0.23}$	$4.48^{+0.43}_{-0.34}$
$R_{\rm cr}$ (pc)	$0 - 5$	LF	$\cdots$	0.46 ± 0.03	0.63 ± 0.06
δ	$0.1 - 10^4$	LF	$\cdots$	940^{+4900}_{-790}	104^{+70}_{-34}
ζ	$10^{-2} - 10^2$	LF (max[ζ,ζ^{-1}])	$\cdots$	$\cdots$	0.78 ± 0.03
$\min(\chi^2_\wp/\nu)$	$\cdots$	$\cdots$	67.66 (541.3/8)	41.22 (247.3/6)	1.65 (8.25/5)
$\min(\chi^2/\nu)$	$\cdots$	$\cdots$	67.61	40.94	1.22

Note. — The values quoted are the median parameter and symmetric quantiles found with the Markov Chain run (as opposed to the single best fit).

[a]F is flat, LF is log-flat, and N is a normal distribution.

[b]The lower bound on distance is taken from Hannikainen et al. (2009), and the upper is derived using $D \leq \frac{c}{\sqrt{\mu_a \mu_r}}$ (Mirabel & Rodríguez 1999).

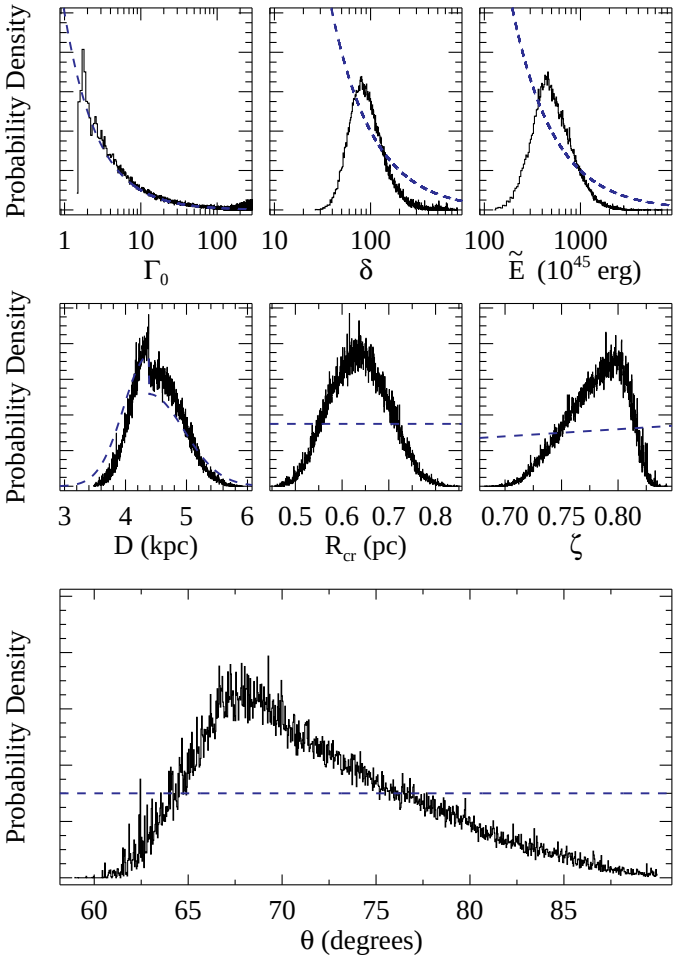

Fig. 3.— MCMC results for Model AC. Probability densities are shown for each parameter to an arbitrary scale. An overlay for each prior shape is drawn as a blue dashed line. Note that the only two parameters which closely track the prior function are the system distance and Γ_0 (at high values only). Otherwise, the prior contributes minimally to the parameter distribution.

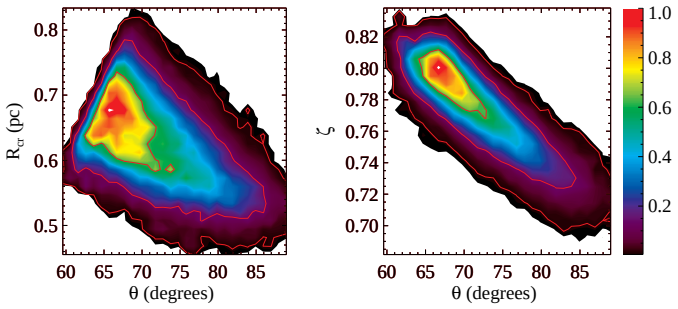

Fig. 4.— Density contours of the MCMC results for Model AC show the two prominent correlations with inclination: cavity size and the cavity asymmetry measure. Red contours mark the 1, 2, and 3σ confidence regions about the most likely value, which is normalized to give a density of 1. The central value of θ changes from 70–80° as $R_{\rm cr}$ varies from 0.65 pc to 0.58 pc, and when ζ decreases from 0.78 to 0.74.

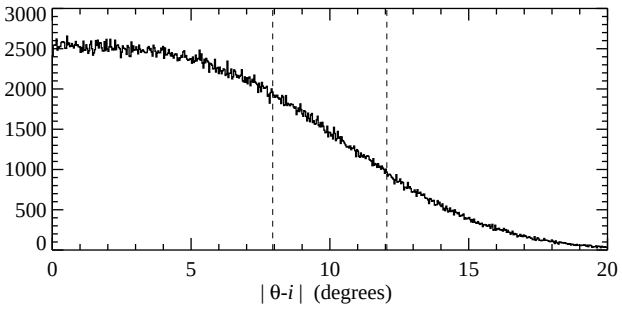

Fig. 5.— The misalignment estimate derived from the MCMC run of Model AC. The results show that no misalignment is likely for J1550; 1σ and 90% upper limits are measured at $\approx 8°$ and 12° respectively.

To now test the viability of an asymmetry in the jets rather than asymmetry in the cavities, we set $\zeta = 1$ and free η. We refer to this model as Model RAJ (Model AJ for the kinematic formulation in which no radio intensities are used). In addition to Δ, an additional parameter q is used to describe the effect of the asymmetry on the radio jets. The results for fitting with both models are reported in Table 3. Model RAJ is equally successful at fitting the data, but achieves a worse $\chi^2_\wp/\nu$ because it comes with one additional free parameter. The model implies a higher inclination $\theta \approx 82^\circ$, and also implies a very large intrinsic asymmetry, a factor $\sim 15(= 1/\eta)$. In addition, the fact that q is near 0 implies that the asymmetry measure is attributable to a difference in the ambient gas density and is not as likely to be an asymmetry in either the jet energy or opening angle.

From consideration of the goodness-of-fit to the data including radio intensity measurements, we find that there is no reason to prefer an asymmetric cavity model over one in which the jets (or ambient density) is asymmetric between east and west. However, a more direct comparison is possible by returning to the kinematic models and deriving a comparison between Model AC and Model AJ. In this case, both models have seven parameters, and also an identical structure for the prior, with one asymmetry term replaced for another. Because we attribute equal likelihood to both forms of asymmetry, we can use the penalty normalization from our nominal model, Model AC, and apply it to Model AJ. These results are given in Table 3, and from the difference in $\chi^2_\wp$: $\min(\chi^2_{\wp,\mathrm{AJ}})-\min(\chi^2_{\wp,\mathrm{AC}}) = 3.6$, we find that Model AJ is less likely at the 90% level of confidence.

We conclude that unlike the jets of GRO J1655 where asymmetries of some kind must produce reversing intensity variations, J1550 is consistent with symmetry in the eastern and western jets. Instead, we attribute asymmetry in the system to the presence of a lopsided evacuated cavity encasing the black hole.

7. Discussion

Heinz (2002) have proposed that based upon large-scale motions ~ 0.1 pc observed from a handful of microquasars, that black-hole binaries many generally inhabit low density environments, or alternatively that they reside in bubbles filled with low density gas. Our work, as well as the previous studies of J1550, lend strong credence to this suggestion for J1550. Heinz proposes that the cavity may be an approximately spherical remnant of the progenitor supernova explosion, or alternatively that the cavity may be a collimated channel maintained by e.g., a kinetic outflow like an accretion disk wind or persistent jet (also, see Hao & Zhang 2009). For the latter explanation to hold true, the activity should be near-continuous, or else there must be very little proper motion in the system to prevent the

Table 3. Additional Kinematic Model Results

Parameter	Model AJ	Model RAC	Model RAJ
θ (degrees)	$86.2^{+2.4}_{-3.1}$	$72.8^{+7.4}_{-5.4}$	$81.9^{+5.1}_{-6.8}$
Γ_0	22^{+270}_{-19}	37^{+390}_{-33}	$1.41^{+0.33}_{-0.14}$
$\tilde{E}$ (erg)	213^{+83}_{-65}	$6.1^{+3.8}_{-2.3}$	80^{+30}_{-34}
D (kpc)	4.83 ± 0.36	$4.49^{+0.43}_{-0.35}$	$3.57^{+0.50}_{-0.44}$
$R_{\rm cr}$ (pc)	0.46 ± 0.05	0.63 ± 0.06	$0.35^{+0.04}_{-0.05}$
δ	510^{+1700}_{-410}	98^{+57}_{-30}	740^{+3300}_{-590}
ζ	$\cdots$	0.78 ± 0.03	$\cdots$
η[a]	0.065 ± 0.014	$\cdots$	$0.068^{+0.016}_{-0.013}$
Δ[b]	$\cdots$	$1.9^{+3.2}_{-1.1}$	$1.8^{+5.3}_{-6.5}$
q[b]	$\cdots$	$\cdots$	$-0.28^{+0.52}_{-0.35}$
$\min(\chi^2_{\wp}/\nu)$	2.37 (11.83/5)[c]	1.38 (8.31/6)	1.43 (7.16/5)
$\min(\chi^2/\nu)$	1.11	1.11	1.31

Note. — The values quoted are the median parameter and symmetric quantiles found with the Markov Chain run (as opposed to the single best fit).

[a]The form of the prior for ζ and η are identical (see Tab. 2).

[b]A flat prior is used for both Δ and q. The former is allowed to take values between [-10,10] and the latter is constrained to the range [-1,2].

[c]The penalty normalization for Model AJ is derived originally for Model AC.

cavity structure migrating substantially.

We further remark upon a notable feature of our model: X-ray emission is detected only after jets reach scale of the western cavity (Fig. 2). However, the eastern jet is detected in X-rays before reaching the eastern cavity wall. It may be that the cavities are naturally truncated by proper motion, to approximately the scale we observe, or else it may be that the cavity walls themselves are porous, and that filaments of matter breach the cavity and produce X-ray emission in advance of the stronger shocks at the cavity boundary.

The total enthalpy of these cavities is of order $10^{40}-10^{42}$ erg, a scale easily maintained by steady or frequent injections from small-scale jets while the system is in a hard or quiescent state (Remillard & McClintock 2006). The asymmetry is unlikely to be attributed to a large-scale proper motion of J1550 because of the tremendous speed implied ($\sim 0.1c$), but instead is easily explained by a comparably moderate ($\sim 20\%$) pressure or density gradient across the pc-scales spanned by the jets, in a dense region of the Galaxy.

We note that while we have identified asymmetric cavities, the direction of the asymmetry is opposite that measured by Hao & Zhang (2009). We attribute this difference to several divergences in our analyses from theirs: First, they pre-assumed values for θ, $\tilde{E}$, and Γ_0 and also used a large asymmetry term (equivalent to $\eta^{-1} \approx 30$), large enough that their $\zeta = 1.4$ would have compensated in the other direction. We were able to substantially improve the data set, and in our analysis found no need for an extreme asymmetry at all.

Lastly, we find that the total energy associated with the jets $2 \times \tilde{E} \approx 10^{46}$ erg, is consistent with the mass accreted onto J1550 during its day-long ejection event being diverted into fueling the impulsive jets: Because J1550 has $a_* \approx 0.5$, and was near its Eddington rate during the X-ray flare (Steiner et al. 2011), the rate of mass flowing through the disk would have been $\dot{m} \sim 10^{19}$ g s^{-1}, providing an accumulated $\sim 10^{24}$ g. Allowing that this is all subject to an order-of-magnitude uncertainty, the accreted mass and energy of the jet are well matched for $\Gamma_0 \approx 10$, well within the range of our measurements. This implies that much or all of the accreted mass was used to power the jet, or alternatively that the energy in the jet was comparable to that accreted during the launching event.

8. Conclusion

Building upon work by Hao & Zhang (2009) and Wang, Dai, & Lu (2003), we have modeled the kinematic motion of the ballistic jets of J1550 using *Chandra* and radio images in order to determine the degree of alignment between the spin-axis (that of the jets) and the binary orbit. We find that the spin axis is highly inclined, $\theta > 65°$, and is consistent

with either zero or minor tilt ($< 8°$) with respect to the binary orbital plane.

JFS was supported by the Smithsonian Institution Endowment Funds and JEM acknowledges support from NASA grant NNX08AJ55G. We thank Bob Penna, Sasha Tchekovskoy, and Ramesh Narayan for constructive ideas which helped shaped the direction of this work.

REFERENCES

Bardeen, J. M., & Petterson, J. A. 1975, ApJ, 195, L65

Blandford, R. D., & McKee, C. F. 1976, Physics of Fluids, 19, 1130

Chaty, S., Charles, P. A., Martí, J., Mirabel, I. F., Rodríguez, L. F., & Shahbaz, T. 2003, MNRAS, 343, 169

Corbel, S., Fender, R. P., Tzioumis, A. K., Tomsick, J. A., Orosz, J. A., Miller, J. M., Wijnands, R., & Kaaret, P. 2002, Science, 298, 196

Fabian, A. C., Rees, M. J., Stella, L., & White, N. E. 1989, MNRAS, 238, 729

Fragos, T., Tremmel, M., Rantsiou, E., & Belczynski, K. 2010, ArXiv e-prints

Gelman, A., Roberts, G., & Gilks, W. 1996, in Bayesian Statistics, ed. J. M. Bernado et al., Vol. 5 (OUP), 599

Gelman, A., & Rubin, D. 1992, Statistical Science, 7, 457

Hannikainen, D. C., et al. 2009, MNRAS, 397, 569

Hao, J. F., & Zhang, S. N. 2009, ApJ, 702, 1648

Hastings, W. 1970, Biometrika, 97

Heinz, S. 2002, A&A, 388, L40

Hjellming, R. M., & Rupen, M. P. 1995, Nature, 375, 464

Hjellming, R. M., et al. 2000, ApJ, 544, 977

Huang, Y. F., Dai, Z. G., & Lu, T. 1999, MNRAS, 309, 513

Kaaret, P., Corbel, S., Tomsick, J. A., Fender, R., Miller, J. M., Orosz, J. A., Tzioumis, A. K., & Wijnands, R. 2003, ApJ, 582, 945

King, A. R., Lubow, S. H., Ogilvie, G. I., & Pringle, J. E. 2005, MNRAS, 363, 49

Lodato, G., & Pringle, J. E. 2006, MNRAS, 368, 1196

Maccarone, T. J. 2002, MNRAS, 336, 1371

Martin, R. G., Pringle, J. E., & Tout, C. A. 2009, MNRAS, 400, 383

Martin, R. G., Reis, R. C., & Pringle, J. E. 2008a, MNRAS, 391, L15

Martin, R. G., Tout, C. A., & Pringle, J. E. 2008b, MNRAS, 387, 188

Martínez, V. J., Saar, E., Martínez-González, E., & Pons-Bordería, M.-J., eds. 2009, Lecture Notes in Physics, Berlin Springer Verlag, Vol. 665, Data Analysis in Cosmology

Mirabel, I. F., & Rodríguez, L. F. 1999, ARA&A, 37, 409

Natarajan, P., & Pringle, J. E. 1998, ApJ, 506, L97

Orosz, J. A., et al. 2001, ApJ, 555, 489

—. 2009, ApJ, 697, 573

Orosz, J. A., Steiner, J. F., McClintock, J. E., Torres, M. A. P., Remillard, R. A., Bailyn, C. D., & Miller, J. M. 2011, ApJ, 730, 75

Özel, F., Psaltis, D., Narayan, R., & McClintock, J. E. 2010, ApJ, 725, 1918

Remillard, R. A., & McClintock, J. E. 2006, ARA&A, 44, 49

Reynolds, C. S., & Nowak, M. A. 2003, Phys. Rep., 377, 389

Sobczak, G. J., McClintock, J. E., Remillard, R. A., Cui, W., Levine, A. M., Morgan, E. H., Orosz, J. A., & Bailyn, C. D. 2000, ApJ, 544, 993

Steiner, J. F., et al. 2011, arXiv:astro-ph/1010.1013

Stetson, P. B. 1987, PASP, 99, 191

Tingay, S. J., et al. 1995, Nature, 374, 141

Verde, L., et al. 2003, ApJS, 148, 195

Wang, X. Y., Dai, Z. G., & Lu, T. 2003, ApJ, 592, 347

Zhang, S. N., Cui, W., & Chen, W. 1997, ApJ, 482, L155